RSC Advances

ROYAL SOCIETY OF CHEMISTRY

www.rsc.org/advances

Evaluating the Merit of ALD Coating as Barrier against Hydrogen Degradation in Capacitors Components

Damoon Sohrabi Baba Heidary*, Weiguo Qu, Clive A. Randall

Center for Dielectrics and Piezoelectrics, Materials Research Institute, the Pennsylvania State University, University Park, Pennsylvania 16802, USA

Corresponding Author: Damoon Sohrabi Baba Heidary

(917) 376-7737, dus255@psu.edu

Abstract

The degradation of properties of electronic materials due to exposure to hydrogen gas is a common problem in electro-ceramic device components. In this study, we explore atomic layer deposition (ALD) coatings as a potential barrier against hydrogen gas. Three ALD chemistries of ZnO, Al_2O_3, and HfO_2 with different thicknesses were coated onto $BaTiO_3$ capacitors, and their merit as hydrogen gas barriers at high temperatures was evaluated by I-V and impedance spectroscopy that could monitor the degradation of resistivity. Those experimental investigations provide the temperature of merit (T_0) and the proton (H-ion) diffusion coefficients of the ALD layers, which can be used to evaluate their barrier effectiveness. Transmission electron microscopy (TEM) analysis was applied to examine the ALD layers before and after the I-V tests and find out the physical dimensions, conformity, and structure (amorphous and crystalline) of the ALD layers. We determine that the failure of the barrier characteristics at elevated temperatures is due to crystallization. The diffusion coefficient associated with protons before and after crystallizations in ALD layers was determined. Within the chemistries investigated here, the most effective ALD layers are made of HfO_2 with amorphous structure.

Keywords: ALD, hydrogen, gas barrier, crystallization, diffusion, TEM

1. INTRODUCTION

Hydrogen gas exposure to a $BaTiO_3$ based dielectric material can dramatically decrease resistivity. This is believed to be associated with H^+ ions (protons) accumulating in interfacial regions, and in the case of n-type doped semiconductors, makes the Schottky barriers more conductive. This could be a potential problem in packaging modules for power electronics [1], as outgassing of hydrogen or related gases will raise the activity of H_2 in the sealed modules. This can gradually impact capacitors and other interfacial controlled devices that control voltage and current, such as varistors and positive temperature coefficient of resistance (PTCR) components, inducing early lifetime failures of the components and possibly catastrophic system failures [2–5]. The resistivity degradation of multilayer $BaTiO_3$ dielectrics structure has been studied by a number of other reports [6,7]. In contrast to those oxygen vacancy controlled time dependent break down processes [8–10], the effects of H^+ has been rarely considered. In our recent investigations of the effects of H^+, it was demonstrated that there are major changes that significantly reduce the electrode Schottky barrier width, especially at the electrode interfaces, as determined by combined in-situ impedance spectroscopy and I-V analysis [6,7].

The objective of this investigation is to determine if there is a potential for effective use of atomic layer deposition (ALD) coatings to limit the insulation degradation due to hydrogen gas on base metal electrode (BME) $BaTiO_3$ capacitors [11–13]. ALD coatings have already been identified as diffusion barriers in a number of applications[14–1617], such as prohibiting copper diffusion to dielectrics in the backend copper interconnects [18,19], or as a gas diffusion barrier on Kapton and PEN (Polyethylene Naphthalate) polymers [11]. The effectiveness of ALD as a diffusion barrier is significant for those polymers; for example, it has been shown that a 10nm alumina ALD can reduce the water vapor transmission rate by 3 orders of magnitude [20,21]. The gas barrier property of oxides is due to the strong bond between hydrogen and oxygen, which considerably increases activation enthalpy for proton diffusion in oxides. [22]. Norby et al. [23] have reviewed hydrogen diffusion in different oxides.

ALD consists of two half reactions that conformally coat a layer with atomic precision on a surface [24–26]. For example, ALD reactions for alumina are made of two half reactions [27]:

$$Al-OH^* + Al(CH_3)_3 \longrightarrow Al-O-Al-(CH_3)_2^* + CH_4$$
$$Al-CH_3^* + H_2O \longrightarrow Al-OH^* + CH_4 \quad (1)$$

where the asterisks indicate the surface species. Both reactants, namely, Trimethylaluminum (TMA), $Al(CH_3)_3$, and water are in a gas phase. Both reactions are self-terminating, i.e., after the first atomic

layer, the reactions stop automatically and are exothermic enough to continue spontaneously. These features are essential in ALD reactions[28].

ALD coatings have several features that make them a unique technique for coating barrier layers. Since the ALD reactions can be separated into two independent and self-terminating half-reactions, the coatings have high aspect ratio, which leads to a conformal, continuous, and flawless coating, with an even thickness all around samples [11,28].

In this paper, it has been shown that ALD coating can be deposited on $BaTiO_3$. Their barrier properties were studied while the samples were exposed to hydrogen gas with I-V tests and impedance spectroscopy to measure the temperature of merit (T_0) and diffusion coefficient in ALD layers. Diffusion coefficient in ALD coating can be a quantitative criteria to show how effective an ALD layer is against hydrogen or be useful in the study of oxide layer degradation due to exposing to hydrogen gas in MOS devices [29,30]. TEM analysis has also been executed to study the structure of the layers before and after exposing to hydrogen gas at high temperature.

2. EXPERIMENTAL SECTION

Model capacitor structures were fabricated with typical cofired methods [31]. $BaTiO_3$ powders co-doped with Y_2O_3-MnO X7R formulations, were tape casted into layers with thickness of 50 and 20 µm and cut to the 1×1 inch squares. The electrodes patterns, 4×5 rectangles with the dimensions of 2×4.5 mm, were printed with a homemade nickel ink (made with Shoei Chemical Ni powder) on the two of 20-µm squares. Tapes and electrodes were aligned so that every rectangle had an overlap area of 2×2.5 mm and an extent of 1 mm in both sides in its length direction. After a satisfactory alignment, those 20 µm layer were stacked with six 50-µm squares on the top and the bottom and then were laminated, cut to separate rectangles, and sintered at 1300°C for 2 hours in 10^{-10} atm of oxygen partial pressure. After that, the samples were reoxidized at 800°C in 10^{-8} atm of oxygen partial pressure for 8 hours. The final products were test capacitor structures, which had one active layer with 18 µm thickness, with high quality dielectric performance. To make sure hydrogen would be exposed in the same way to the active layer in all the samples, they were cut along the electrode, as shown in Figure 1 (a), and hydrogen effects could be noted over relatively accelerated conditions.

Before the ALD process, the samples were placed in a supersonic bath of acetone for 5 minutes, followed by another 5 minutes in isopropyl alcohol, and dried in an oven for 20 minutes at 120 °C to make sure all the surface contaminations were removed. Then they were coated with an ALD system

(150LE, The Kurt J. Lesker Co.) with the recipes shown in Table 1. The samples were coated with 220, 440, 660, and 880 cycles. The schematic of ALD coated sample is shown in Figure 1 (b). In this paper, the number of cycles instead of thickness will be used. Since every cycle takes roughly 20 seconds, the number of cycles represents the processing time for ALD coatings. One can convert the cycles to the thickness by the average growth rates, reported in Table 1. (However, it will demonstrate thickness does not play a fundamental role in barrier property of the coatings.)

Before and after ALD coating the sample, capacitance and loss were measured by HP4284A LCR meter (Hewlett-Packard) at 1 V to make sure that their electrical properties did not change before and after ALD.

The I-V tests were used to assess the merit of coating in forming gas (4% hydrogen and 96% nitrogen) in the temperature interval of 150 to 300 ^{o}C. A furnace with sealed stainless steel inside was used to heat samples. Forming gas could be blown inside the box, and temperature could be measured accurately with a K-type thermocouple embedded inside the box. The temperature was ramped with 10 ^{o}C step, each sample was charged by HP4140B PA meter (Hewlett Packard) to 15 V for 60 seconds, and leakage current was recorded at every second and then discharged for another 60 seconds. This process was repeated three times at each temperature to make sure stable numbers were being measured. The final leakage current was measured for each temperature, roughly after 25 minutes of being at that temperature. Two samples without coatings were tested in air and forming gas as references for no degradation and complete degradation states, respectively. Forming gas would be called hydrogen atmosphere from now on.

Impedance spectroscopy was applied by using SR-830-DSP Lock-in connected to homemade charge measurement hardware to measure the proton diffusion coefficient in ALD layers. The impedance tests were executed in the frequency range of 10 kHz to 0.01 Hz with ac voltage of 0.1 V at temperatures of 235, 245, and 255 ^{o}C.

TEM samples were prepared by FEI-Quanta-200 FIB (Oregon, USA). TEM micrographs were done by JEOL-2010 field emission TEM (Tokyo, Japan).

3. RESULTS AND DISCUSSION

Saturate leakage currents vs. temperature for samples without coating are shown in Figure 2 (a) at air and hydrogen atmosphere. As described in details in previous paper[7], hydrogen ions cause a resistivity degradation in $BaTiO_3$ capacitors. As shown in Figure 2 (a), the leakage current difference between the two typical samples in air and hydrogen atmosphere becomes obvious around 160 ^oC. Those curves are shown in the other graphs of Figure 2 and can be used as the indicators of two extreme conditions, from no protection to full protection against hydrogen gas damage.

Figure 2 (b) shows the results of the I-V test for the samples coated with 220 to 880 cycles of Al_2O_3. As long as the measured leakage current for the coated samples is close to the leakage currents for the uncoated sample in air, it would be assumed that the ALD coating is fully protecting the samples against hydrogen gas, and the first departure from the 'air' curve would be considered as the failure of the coating against hydrogen. Thus, one would be able to define a temperature, below which the samples are fully protected against hydrogen, would be called temperature of merit (T_0) in this paper. T_0 is shown in Table 2 for Al_2O_3 coatings. The highest T_0 is 270 ^oC and has been obtained at 660 cycles, while T_0 is 260^oC for 880 cycles. Plus, the fact that the measured leakage current is much higher for 880 cycles at 300^oC than 660 or even 440 cycles, suggests that the thicker coatings do not necessarily provide better protection, and rather, there is an optimum thickness. This phenomenon would be discussed more by using TEM analysis.

The leakage currents for the samples with HfO_2 coatings are given in Figure 2 (c) and T_0 in Table 2. As can be seen, there is not much difference between 220 to 880 cycle coatings up to 300 ^oC. To find out how high T_0 is, the maximum temperature was extended to 350 ^oC, and the sample with 110 cycle thickness was also tested. It can be seen in Table 2 that all the thicknesses above 110 cycles have T_0 of 310^oC. The sample with 110 cycle coating has T_0 of 290^oC. As found for Al_2O_3 coatings, the lowest leakage current at 350^oC is for the sample with 660 cycles. However, the differences are not as large as with the Al_2O_3 coatings.

The ZnO ALD was, comparatively, not as good a barrier against hydrogen ions under the deposition condition used here. The 660 and 880 cycle coatings change the sample resistivity before and after ALD coating. The best results were obtained in 440 cycles, which has been compared with Al_2O_3 and HfO_2 440 cycles in Figure 2 (d). The T_0 would be 230 ^oC for ZnO coating, which is the lowest among other ALD coatings. HfO_2 shows the best barrier property against hydrogen gas.

It should be pointed out that since the different components have different growing rates as shown in Table 1, after 440 cycles, they have different thicknesses. As will be demonstrated later, the thicknesses are 40, 48, and 57 nm for Al_2O_3, HfO_2, and ZnO respectively. As mentioned in the experimental section, the number of cycles is representative of processing time. So Figure 2 (d) basically shows that by spending of same amount of processing time, one can obtain much better gas barrier by using HfO_2 instead of the other compounds. Number of cycles is suitable variable to compare different ALD coatings, since one of the ALD disadvantage is mentioned to be a time consuming process and it draws this conclusion that by using more stable compound one would be able to obtain a better barrier layer by spending the same processing time.

Furthermore, the coating thickness does not have a fundamental contribution to the barrier property of ALD coatings; as shown in Figure 2 (c), the leakage currents do not change below T_0 for the coating with cycle number, higher than 110. This is true for Al_2O_3 coating with the cycle number, higher than 220. Thus, the comparison of the ALD coatings with 440 cycles is quite reasonable.

Boiling and melting temperatures can be criteria of the bond strength of chemical compounds. Since the atomic bonds will break during evaporation, higher boiling temperature means stronger bond between atoms. So one would be able to compare the ALD coating stability with each other by knowing their boiling temperatures. The ZnO, Al_2O_3, and HfO_2 have boiling points of 1975 [32], 2980 [33], and 5100^{o}C [34], respectively. So HfO_2 is the most stable oxides among the others. One can arrive to the same conclusion by comparing their melting points, or their bond dissociation enthalpy. Hf-O, Al-O, and Zn-O have the bond dissociation enthalpy of 801, 502, 250 kJ/mol[35], respectively.

This is possibly why HfO_2 is the best barrier coating among the others. Yesibolati[36] demonstrated that HfO_2 can be used as an effective surface passivation. Huang showed that HfO_2 shows better stability and barrier property than Al_2O_3[37]. On the contrary, ZnO has the lowest boiling point, which is the least stable structure and having the minimum barrier property among the others.

Figure 3 shows the TEM micrograph of Al_2O_3 coatings with 220, 660, and 880 cycles along with the energy dispersive spectroscopy (EDS). ALD coatings, as expected, are flawless, continuous, and conformal, as shown in Figure 3 (a) in a low magnification. The ALD layers of 220, 660, and 880 cycles have been shown in higher magnification in Figure 3 (b) to (d). Their thicknesses are respectively measured between (17, 20), (57,63), and (75, 79) nm for the 220, 660, 880 cycles, which suggested the average growth rate of 0.9 $\dot{A}$ per cycle. Since the original samples were made by sintering of $BaTiO_3$

powder and they have rough and porous surfaces, the fluctuation in thickness was expected. Furthermore, it was proven that Al_2O_3 layers are amorphous by SAED (selected area electron diffraction) patterns. The gold layers, shown in Figure 3, were coated on the samples during the sample preparation process.

The EDS analysis was executed across the layers in Figure 3 (d), and the result for Au, Al, and Ba vs distance are shown in Figure 3 (e). It proves the layers are labeled correctly in Figure 3 (d).

The ALD coating is effective because both precursors are in gas phase; they can diffuse to the sample and fill the interconnected porosities and the empty space between grains and electrode interfaces. An example of a $BaTiO_3$ grain, enclosed with ALD coating, can be found in Figure 3 (a), where the arrow is pointing. As a matter of fact, the precursor diffusion is not limited to the surficial grains; they can diffuse inside the capacitors and fill the open interconnected porosities. For example, during TEM analysis, a hole 4.8 μm beneath the surface and near to electrode was found partially filled with alumina. That can be considered as an advantage for ALD coatings, because precursors can fill the holes near the surface and form a continuous coating on the top of the surface, providing a true sealing for the samples against hydrogen gas.

The next insight that can be found by TEM analysis is why ALD coatings fail after T_0. Figure 4 shows the 80 nm Al_2O_3 layer after the I-V test. As seen in Figure 4 (a), some portion of ALD layer is crystallized and surrounded by an amorphous structure. The crystallized part looks like a nucleus in the early state of growth. Figure 4 (b) shows a bigger crystallized region, with the grain boundary between crystallized and amorphous area. It looks like a fully grown columnar grain, which reach the upper and lower interfaces. One can see the primary and the final states of grain crystallization from the amorphous region through Figure 4 (a) and (b).

Figure 4 (c) shows the crack-like features due to the internal stress of ALD coating, caused by the crystallization. However the dominant faults were grain boundaries between crystallized and amorphous regions. These features offer an easy path for hydrogen ions to diffuse into the capacitors, and this is the main reason for ALD layer failure after T_0.

Those grain boundaries were much less in 660 cycle ALD layer, so it may be the reason that the leakage current is much higher in 880 cycle than 660 and 440 cycle at 300 ^oC, as shown in Figure 2(b). Since the leakage current is also slightly higher for 880 cycle than 660 and 440 cycle in HfO_2 layers at 350^oC, as shown in Figure 2(c), one can conclude, based on those curves, that the coatings with 880

cycles are less stable than the 660 and 440 cycles in both Al_2O_3 and HfO_2 at high temperatures. In other words, the thicker coatings become crystallized more easily in high temperature than the thinner ones, and above T_0, the total proton diffusion mostly depends on the crystallization percentage and the number of grain boundaries, and not on the layer thicknesses. Jen et al.[38] have shown thinner Al_2O_3 ALD coatings are more mechanically robust against cracking than the thicker ones.

The TEM micrograph of the HfO_2 coated samples with 880 cycle coating before and after I-V tests along with SAED patterns is shown in Figure 5. It suggests exposure to high temperature, 350°C, introduces crystallized portion and grain boundaries to HfO_2 layers, too.

There is an obvious region with coarse Moiré fringes, which is the sign of two crystallized planes that translate or/and rotate against each other [39] in Figure 5 (b), shown with 'A'. There are other regions with less obvious fringes, labeled as 'B' and 'C'. They may result from a crystallized and amorphous planes that sit on top of each other. This explanation can be supported by SAED pattern, which was shown in insets. Having both patterns of donut-shape and points indicates the coexistence of crystallized and amorphous regions in the microstructure, shown in Figure 5 (b).

The other feature is Fresnel-contrast, the result of two neighbor regions with different inner potentials, when the image is out of focus [40]. This contrast can be seen in the borders of regions B and C and can be the sign of grain boundaries, which connect the top of ALD layer to the bottom. These types of faults can provide a free path for protons to pass ALD layer and diffuse inside $BaTiO_3$. Although one should be wary not to mistake the artifact for a real feature in TEM micrographs, there is a considerable change before and after exposure to high temperature, so that it rules out the artifact effect. As a conclusion, the same mechanism as the Al_2O_3 failure, which is crystallization due to exposing to high temperature, is the reason of HfO_2 failure.

Since ZnO has the weakest bond strength, and we observe the minimum T_0 among the tested ALD coatings, it is expected to have the maximum amount of crystallization and faults. The TEM micrograph of ZnO ALD layer as coated is shown in Figure 6. The ALD layer is still conformal and continuous, but due to large amount of crystallization and faults, the layer fails to protect the capacitor against hydrogen gas. As mentioned above, the grain boundaries provide a free path for hydrogen diffusion. The layer in Figure 6 has thickness between 112 and 115nm, and the growth rate in average would be 1.3 Å per cycle.

In the previous paper, the proton diffusion coefficients were found for $BaTiO_3$ BME capacitors in bulk, grain boundaries, and electrode interfaces [6]. Considering there is a linear relation between proton concentration of capacitors and their conductivity (inverse of resistivity) [41–44] at a constant temperature, one would be able to find the proton diffusion coefficient in ALD layers by measuring conductivity changes of the coated capacitors during hydrogen exposure. To find the diffusion coefficient, the diffusion system should be first defined.

To get samples degraded, protons need to pass through ALD coating and arrive to the capacitor active layer, see Figure 1 (b). Since they diffuse in just one direction, and ALD layer is thin so that the proton diffusion reaches steady state quickly, one can define the diffusion system in one direction and apply Fick's first law to find diffusion coefficient. Since it has been proved that the ALD layers can act as a gas barrier (Figure 2), it is assumed that $BaTiO_3$ has a higher diffusion coefficient than ALD layer, and there is no hydrogen accumulation beneath ALD layer at the $BaTiO_3$ and ALD interface.

A virgin sample, coated with 95nm HfO_2, was exposed to hydrogen for seven hours while impedance spectroscopy test was executed once in every hour. The entire test was repeated at three temperatures of 235, 245, and 255 ^oC. The resultant Cole-Cole plots are shown in Figure 7 (a). It has been shown that Cole-Cole plots of BME $BaTiO_3$ capacitors can be best fitted by 3RC model [6,9,45]. Since the electrode has the largest loss of resistance due to hydrogen exposer among the other RC's (grains and grain boundaries) [6], it would be more sensitive to proton concentration. Therefore, the electrode conductance was extracted from the Cole-Cole plots and shown in Figure 7 (b) at different time and temperatures. As seen, the data can be fitted by a line with satisfactory R-squares.

From our earlier work in measuring proton diffusion coefficients for $BaTiO_3$ capacitors, it was shown that there is the following relation between conductivity (σ) and proton concentration (N) at 245^oC [6]:

$$\sigma = 4.35 \times 10^{-9} + 7.15 \times 10^{-5} N \quad (2)$$

By using Eq. (2), the diffusion flux (J) can be obtained and then by replacing it in Fick's first law, diffusion coefficient can be calculated at 245^oC. The diffusion coefficients can be obtained in the same way for other temperatures and other ALD coatings; the coefficients for virgin (as produced) HfO_2 and Al_2O_3 layers along bulk $BaTiO_3$ [6] are shown in Figure 7 (c). As seen, the diffusion coefficient at 245^oC in $BaTiO_3$

is approximately 3000 and 1000 times higher than HfO_2 and Al_2O_3 coatings, respectively. The activation energy in HfO_2 and Al_2O_3 layers are 2.3 and 2.4 eV in contrast to 0.5 eV in $BaTiO_3$. So protons need to pass a higher barrier to jump from one oxygen atom to another in HfO_2 and Al_2O_3, while in $BaTiO_3$, due to octahedron oscillation and momentary $O-H\cdots O$ bonds, the activation energy is much smaller [23]. This explains why those ALD layers can make a good hydrogen gas barrier.

If the HfO_2 and Al_2O_3 are extrapolated, they intersect with $BaTiO_3$ at 376 and 348 ^oC, which theoretically means that they lose their barrier properties at those temperatures. However, the Al_2O_3 and HfO_2 layers start to crystalize at 260 and 310^oC, and this structural change means they lose their barrier property, far below than those extrapolated temperatures. This is also why the reported diffusion coefficient at 255^oC in Figure 7 (c) deviates from the Arrhenius equation. To show the effect of crystallization, two virgin samples, coated with 95nm HfO_2 and 80nm Al_2O_3, were annealed at 350 and 300^oC for one hour at air. Then the same diffusion measurement tests were executed, and the results are shown in Figure 7 (c) as 'HfO_2 C' and 'Al_2O_3 C'. There is an approximately 50 and 100 times increase in diffusion coefficients in annealed samples at 245^oC, which can be due to the grain boundaries. [46,47,48]

The activation energy for the hydrogen diffusion process in the present materials is given in Table 3, along with some related other materials for comparison. The activation enthalpies (H), and especially pre-exponential factors (D_0), are given in crystalized Al_2O_3 and ZrO_2 for comparison with amorphous counterparts. H and D_0 of HfO_2 were not found in literatures, but ZrO_2 is an adequate replacement, since they have the exact same crystal structure and oxidation state and very close atomic radius and crystal parameters [49]. As suggested by data in Table 3, H and especially D_0 for amorphous structure are much higher than the crystallized structure for the same chemical compound. However, those large pre-exponential factors were expected in amorphous structures, as Faupel et al. [50] have reported that D_0 can be in the range of 10^{-11} to 10^{+19} cm^2/s for amorphous alloys.

The concentration of protons can influence the H and D_0 as well. To show an example, the proton activations for amorphous and crystallized silicon [51,52] are given in Table 3. The amount of H and D_0, respectively, decreases from 2.2 to 1.4 and 10^3 to 10^{-4} by increasing proton concentration from 0.1 to 14 at.% in amorphous silicon. Considering the proton concentration is in the order of ppm in this work [6], the data in Table 3 for ALD layers are physically reasonable. In short, since D_0 is related to entropy of migration, one can expect proton migration in amorphous structure will produce more entropy than the order crystals and make D_0 larger in amorphous structures. In the case of enthalpy (H), there is a spectrum of enthalpies in amorphous structures due to the fact that the interstitial sites are not similar

and have different amount of enthalpies. Protons like to fill lower level of enthalpies at first, so that enthalpies are high at low proton concentration, and then they decrease by increasing proton concentration [53–56].

Now, the difference of activations for amorphous and partially crystallized structures in this work can be explained. D_0 is smaller in partial crystalized structures, because the structure gets partially ordered, and it would reduce the average amount of entropy for proton migration. Less disordered structure leads to smaller D_0. One can arrive at the same conclusion by comparing D_0 of amorphous and crystalized compounds in Table 3. For example, D_0 for amorphous Al_2O_3 from 8.0×10^{12} cm^2/s decreases to 2.4×10^{-3} for fully crystalized Al_2O_3. It goes down to 7.7×10^{10} for partial crystalized Al_2O_3 in our work. Apparently, the amount of ordering in partially crystallized structures is not as much as in crystalized ones, since D_0 is still much higher than in crystallized structures.

H is decreased as well in partial crystalized structures, because grain boundaries can offer a wider space for proton diffusion than amorphous structures and protons need less activation enthalpies to jump. Compare the data in Table 3. The enthalpy decrease is the main reason that partially crystallized structures have higher diffusion rates than amorphous ones.

The above mentioned technique may be used as a quantitative method to evaluate the quality or the stopping power of ALD coatings at different temperatures for comparison between different ALD coatings.

4. CONCLUSION

The stopping or barrier power of ALD coating is mostly determined by their chemical composition; as can be seen, there is a huge difference in performance between ZnO, Al_2O_3, and HfO_2. The Al_2O_3 and HfO_2 ALD coatings have amorphous structure and are both effective barriers, up to the crystallization temperatures that are associated with T_0. It was illustrated that the results of I-V tests can be supported by TEM analysis. The Al_2O_3 and HfO_2 ALD coatings are continuous, conformal, and amorphous below T_0, and they show a high barrier performance, as predicted from I-V results. TEM analysis shows that the grain boundaries, formed at temperatures above T_0, cause a reduction in the barrier performance.

The activation of the proton diffusion was measured in the amorphous and partially crystallized structures. The proton diffusion coefficients in ALD are much smaller than the one in BaTiO3 and this the

main reason that the ALD coatings can stop protons, although their thickness is in order of nanometer. Measuring a lower activation enthalpy (H) in the partially crystalized structures suggests that grain boundaries have higher diffusion coefficient than amorphous structures. Both temperatures of merit (T_0) and diffusion coefficients, respectively, resultant from I-V and impedance spectroscopy tests, can be used as a characterization method to assess the quality and stopping power of ALD coatings.

Acknowledgements

This material is based upon work supported by the National Science Foundation, as part of the Center for Dielectric Studies under Grant No. IIP- 1361503 and 1361571.

References

1 H. Wang, M. Liserre and F. Blaabjerg, *Ind. Electron. Mag. IEEE*, 2013, **7**, 17–26.

2 W. P. Chen, Y. Wang, J. Y. Dai, S. G. Lu, X. X. Wang, P. F. Lee, H. L. W. Chan and C. L. Choy, *Appl. Phys. Lett.*, 2004, **84**, 103.

3 Z. J. Shen, W. P. Chen, K. Zhu, Y. Zhuang, Y. M. Hu, Y. Wang and H. L. W. Chan, *Ceram. Int.*, 2009, **35**, 953–956.

4 R. Waser, *Berichte der Bunsengesellschaft für Phys. Chemie*, 1986, **90**, 1223–1230.

5 S. Aggarwal, S. R. Perusse, C. W. Tipton, R. Ramesh, H. D. Drew, T. Venkatesan, D. B. Romero, V. B. Podobedov and a. Weber, *Appl. Phys. Lett.*, 1998, **73**, 1973.

6 D. Sohrabi Baba Heidary and C. A. Randall, *Acta Mater.*, 2015, **x**, xx.

7 D. Sohrabi Baba Heidary, Q. Weiguo and C. A. Randall, *J. Appl. physic.*, 2015, **117**, 124104.

8 C. A. Randall, R. Maier, W. Qu, K. Kobayashi, K. Morita, Y. Mizuno, N. Inoue and T. Oguni, *J. Appl. Phys.*, 2013, **113**, 014101.

9 G. Y. Yang, E. C. Dickey, C. a. Randall, D. E. Barber, P. Pinceloup, M. a. Henderson, R. a. Hill, J. J. Beeson and D. J. Skamser, *J. Appl. Phys.*, 2004, **96**, 7492.

10 G. Y. Yang, G. D. Lian, E. C. Dickey, C. a. Randall, D. E. Barber, P. Pinceloup, M. a. Henderson, R. a. Hill, J. J. Beeson and D. J. Skamser, *J. Appl. Phys.*, 2004, **96**, 7500.

11 S. M. George, *Chem. Rev.*, 2010, **110**, 111–31.

12 J. S. Ponraj, G. Attolini and M. Bosi, *Crit. Rev. Solid State Mater. Sci.*, 2013, **38**, 203–233.

13 R. L. Puurunen, *J. Appl. Phys.*, 2005, **97**, 121301.

14 Z. Liu, Y. Gong, W. Zhou, L. Ma, J. Yu, J. C. Idrobo, J. Jung, A. H. MacDonald, R. Vajtai, J. Lou and P. M. Ajayan, *Nat. Commun.*, 2013, **4**, 2541.

15 J. Meyer, P. Görrn, F. Bertram, S. Hamwi, T. Winkler, H.-H. Johannes, T. Weimann, P. Hinze, T. Riedl and W. Kowalsky, *Adv. Mater.*, 2009, **21**, 1845–1849.

16 C.-T. Chou, P.-W. Yu, M.-H. Tseng, C.-C. Hsu, J.-J. Shyue, C.-C. Wang and F.-Y. Tsai, *Adv. Mater.*, 2013, **25**, 1750–4.

17 L. Kim, K. Kim, S. Park and Y. Jeong, *… Appl. Mater. …*, 2014, **6**, 6731−6738.

18 H. Kim, C. Detavenier, O. van der Straten, S. M. Rossnagel, a. J. Kellock and D.-G. Park, *J. Appl. Phys.*, 2005, **98**, 014308.

19 H. Kim, C. Cabral, C. Lavoie and S. M. Rossnagel, *J. Vac. Sci. Technol. B Microelectron. Nanom. Struct.*, 2002, **20**, 1321.

20 P. F. Carcia, R. S. McLean, M. H. Reilly, M. D. Groner and S. M. George, *Appl. Phys. Lett.*, 2006, **89**, 031915.

21 M. D. Groner, S. M. George, R. S. McLean and P. F. Carcia, *Appl. Phys. Lett.*, 2006, **88**, 051907.

22 W. Münch, G. Seifert, K. Kreuer and J. Maier, *Solid State Ionics*, 1996, **88**, 647–652.

23 T. Norby, M. Widerøe, R. Glöckner and Y. Larring, *Dalt. Trans.*, 2004, 3012–3018.

24 Y. Widjaja and C. B. Musgrave, *Appl. Phys. Lett.*, 2002, **80**, 3304.

25 H. Kim, *J. Vac. Sci. Technol. B Microelectron. Nanom. Struct.*, 2003, **21**, 2231.

26 W.-M. Li, *Chem. Vap. Depos.*, 2013, **19**, 82–103.

27 L. F. Hakim, D. M. King, Y. Zhou, C. J. Gump, S. M. George and a. W. Weimer, *Adv. Funct. Mater.*, 2007, **17**, 3175–3181.

28 K. Knapas and M. Ritala, *Crit. Rev. Solid State Mater. Sci.*, 2013, **38**, 167–202.

29 N. Rahim and D. Misra, *Appl. Phys. Lett.*, 2008, **92**, 023511.

30 M. Houssa, G. Pourtois, M. M. Heyns and a Stesmans, *J. Phys. Condens. Matter*, 2005, **17**, S2075–S2088.

31 H. Saito and H. Chazono, *Jpn. J. Appl. Phys.*, 1991, **30**, 2307–2310.

32 P. Walker and W. H. Tarn, CRC Press, Boca Raton, 1990.

33 D. L. Perry, *Handbook of Inorganic Compounds, Second Edition*, CRC Press, Boca Raton, 2011.

34 R. C. Ropp, *Encyclopedia of the Alkaline Earth Compounds*, Elsevier, Amsterdam, 2013.

35 Y. R. Luo, *Comprehensive Handbook of Chemical Bond Energies*, CRC Press, Boca Raton, FL, 2007.

36 N. Yesibolati, M. Shahid, W. Chen, M. N. Hedhili, M. C. Reuter, F. M. Ross and H. N. Alshareef, *Small*, 2014, **10**, 2849–2858.

37 M. Huang, ARIZONA STATE UNIVERSITY, 2013.

38 S.-H. Jen, J. a. Bertrand and S. M. George, *J. Appl. Phys.*, 2011, **109**, 084305.

39 D. B. Williams and C. B. Carter., *Transmission Electron Microscopy: A Textbook for Materials Science*, Springer, New York, 2009.

40 D. Clarke, *Ultramicroscopy*, 1979, **4**, 33–44.

41 K. Kaneda, S. Lee, N. J. Donnelly, W. Qu, C. A. Randall and Y. Mizuno, *J. Am. Ceram. Soc.*, 2011, **94**, 3934–3940.

42 K. Kreuer, *Solid State Ionics*, 1999, **125**, 285–302.

43 N. J. Donnelly and C. A. Randall, *J. Am. Ceram. Soc.*, 2009, **92**, 405–410.

44 K. Kreuer, E. Schönherr and J. Maier, *Solid State Ionics*, 1994, **70**, 278–284.

45 H. Chazono and H. Kishi, *Jpn. J. Appl. Phys.*, 2001, **40**, 5624–5629.

46 A. Belonoshko, A. Rosengren, Q. Dong, G. Hultquist and C. Leygraf, *Phys. Rev. B*, 2004, **69**, 024302.

47 W. Maoa, T. Chikadaa, K. Shimura, A. Suzukib and T. Terai, *Fusion Eng. Des.*, 2013, **88**, 2646–2649.

48 D. Khatamian, *Defect Diffus. Forum*, 2010, **297-301**, 631–640.

49 J. Adam and M. D. Rogers, *Acta Crystallogr.*, 1959, **12**, 951–951.

50 F. Faupel, W. Frank, M. Macht, H. Mehrer, V. Naundorf, K. Rätzke, H. R. Schober and S. K. Sharma, *Rev. Mod. Phys.*, 2003, **75**, 237–280.

51 A. Van Wieringen and N. Warmoltz, *Physica*, 1956, **22**, 849–865.

52 W. Beyer, *J. Non. Cryst. Solids*, 1996, **200**, 40–45.

53 V. Naundorf, M. Macht, A. Bakai and N. Lazarev, *J. Non. Cryst. Solids*, 1998, **224**, 122–134.

54 V. Naundorf, M. Macht, A. Bakai and N. Lazarev, *J. Non. Cryst. Solids*, 1998, **252**, 679–683.

55 R. Kirchheim, F. Sommer and G. Schluckebier, *Acta Metall.*, 1982, **30**, 1059–1068.

56 R. Kirchheim, *Acta Metall.*, 1982, **30**, 1069–1078.

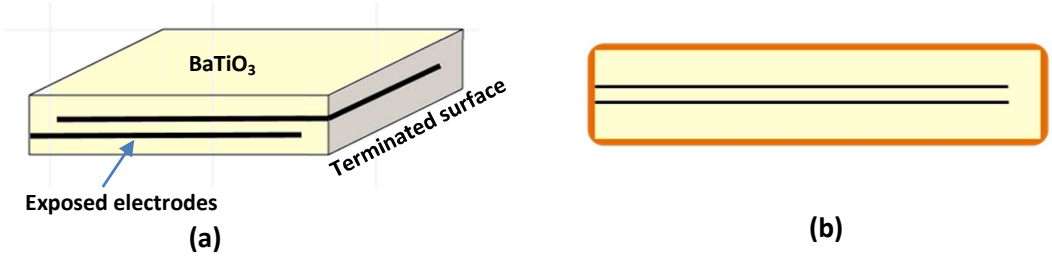

Figure 1 the schematic of (a) cut capacitors, (b) ALD coated capacitor from left view.

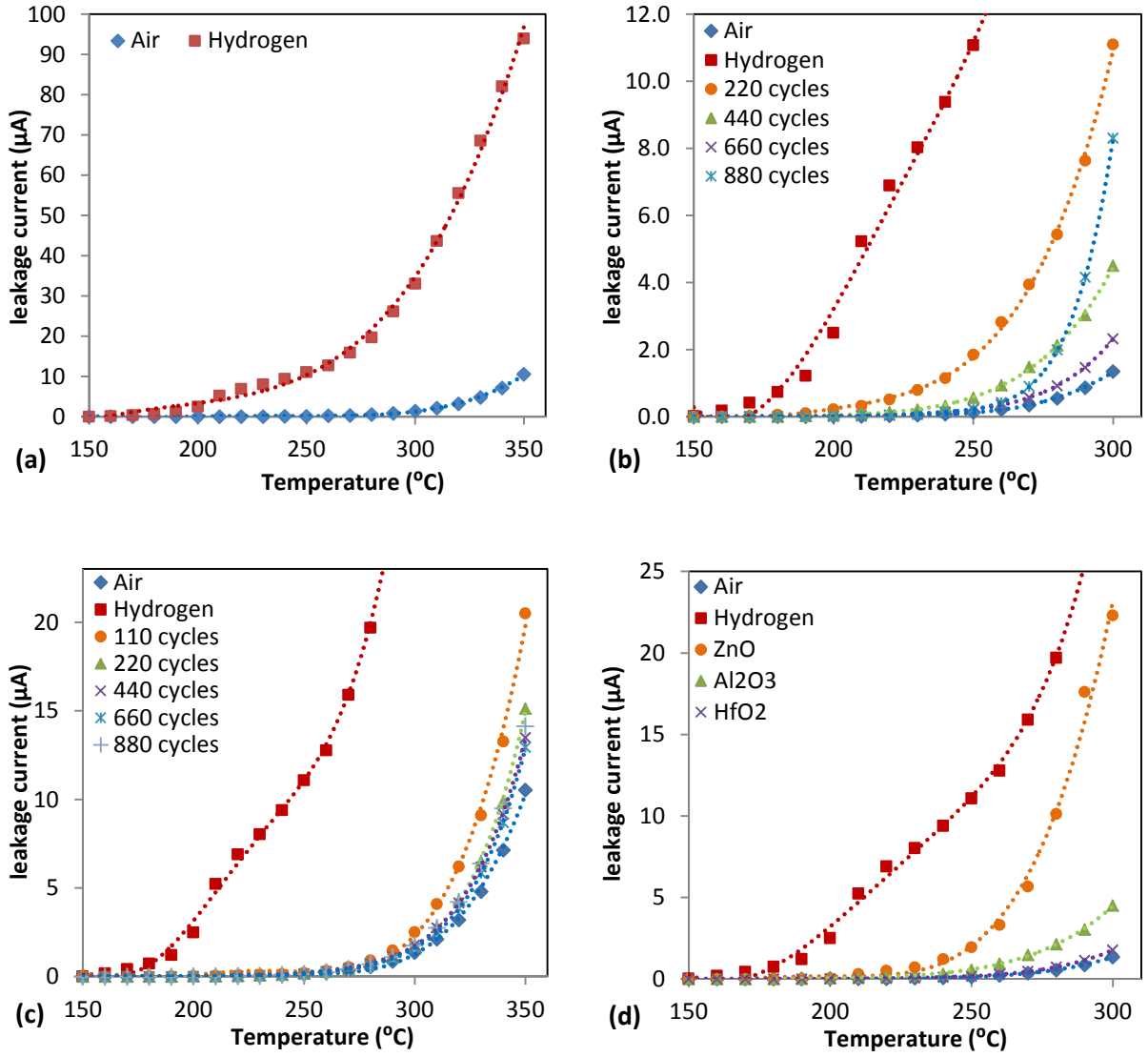

Figure 2. Saturated leakage current vs. temperature for samples (a) without coating in air and hydrogen atmosphere, (b) with Al_2O_3, and (c) HfO_2 coatings at various cycles (d) with different ALD coatings of 440 cycles.

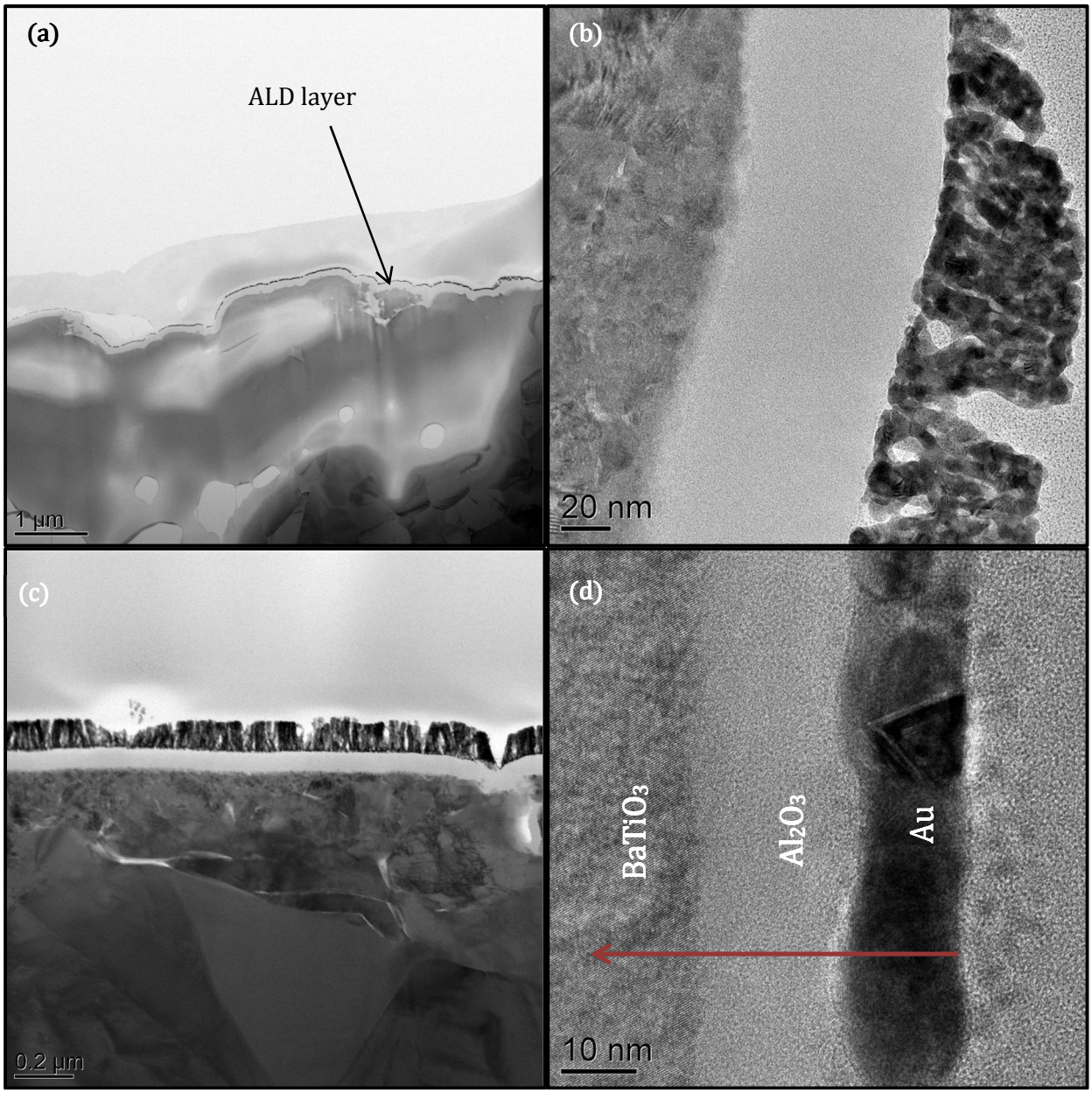

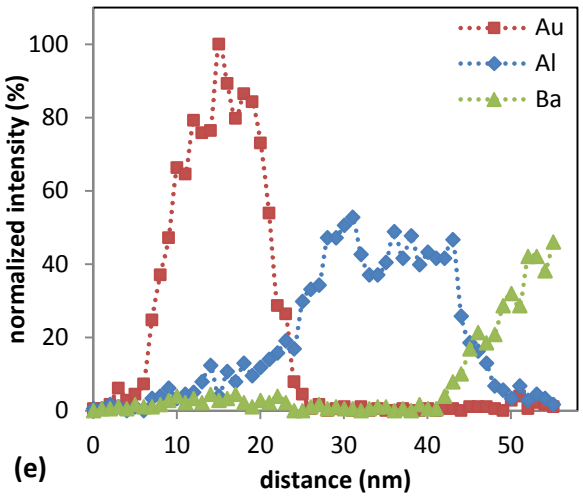

Figure 3 TEM micrographs from samples with Al_2O_3 ALD coating with thickness of (a) and (b) 880 cycles (80 nm), (c) 660 cycles (60 nm), and (d) 220 cycles (20 nm) (e) elemental analysis vs distance cross the layers shown in (d); the arrow shows the path and the direction of the line analysis.

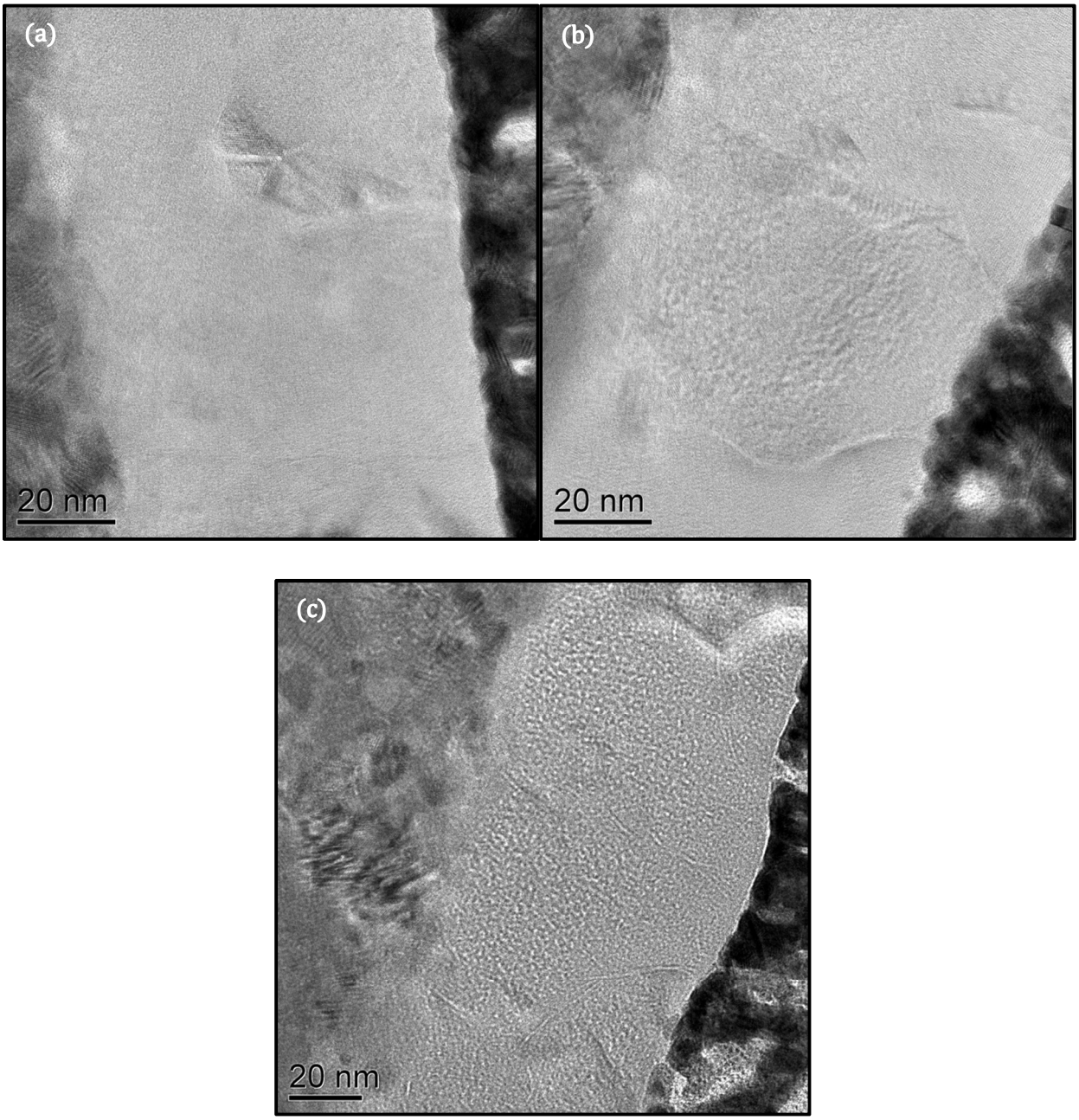

Figure 4 TEM micrographs from the sample with 880 cycles of Al_2O_3 ALD coating after the I-V test, (a) nucleus in the state of growing (b) well devolved crystalized grain with boundaries with amorphous region, (c) mismatch or cracks in ALD layer because of crystallization.

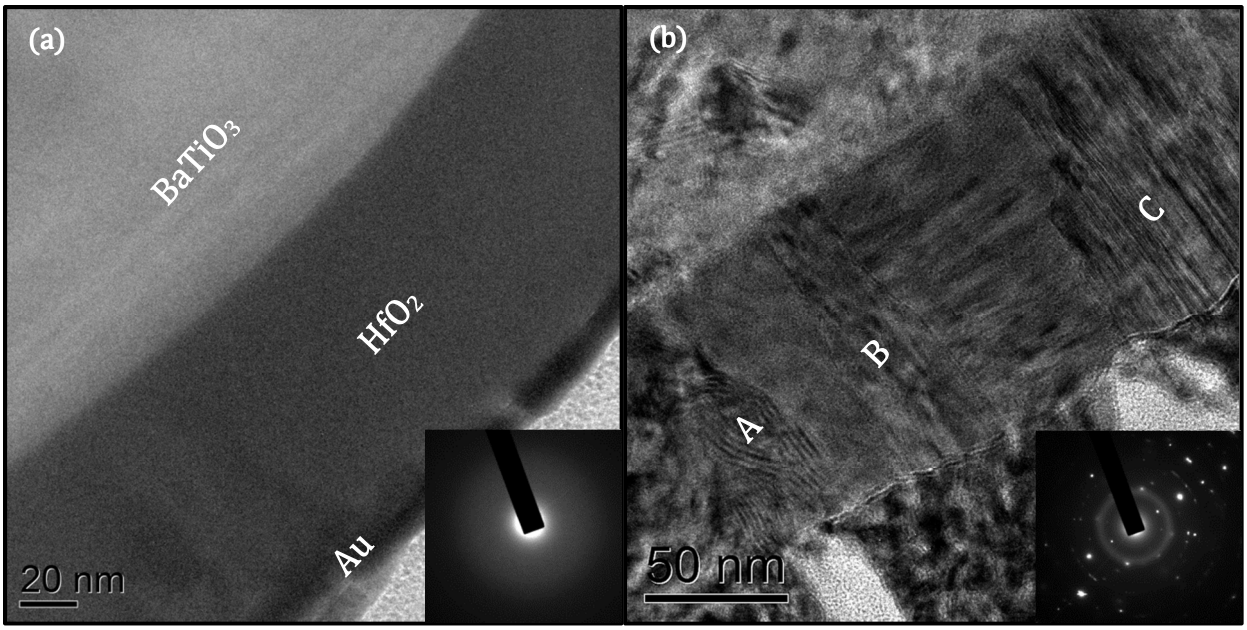

Figure 5. TEM micrographs of the sample with HfO_2 ALD coating (a) before (b) and after I-V tests, A is the region with obvious moiré fringes, B and C are regions with obvious Fresnel-contrast boundaries.

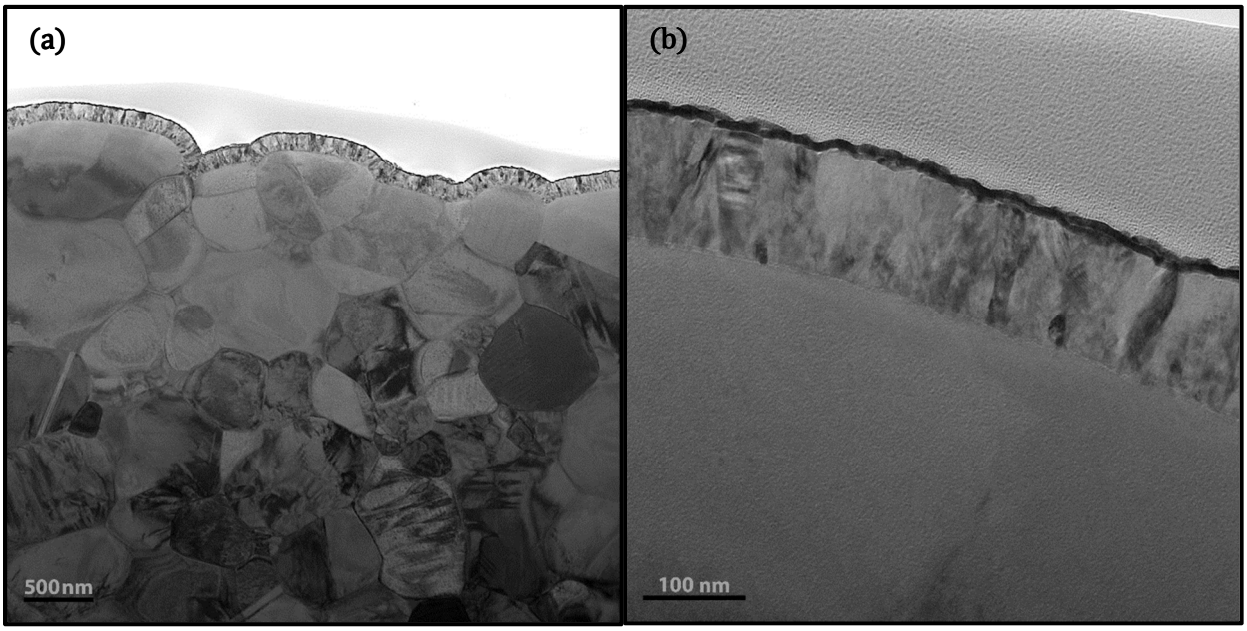

Figure 6 TEM micrographs from the sample with 880 cycles of ZnO ALD coating as coated in two different magnifications.

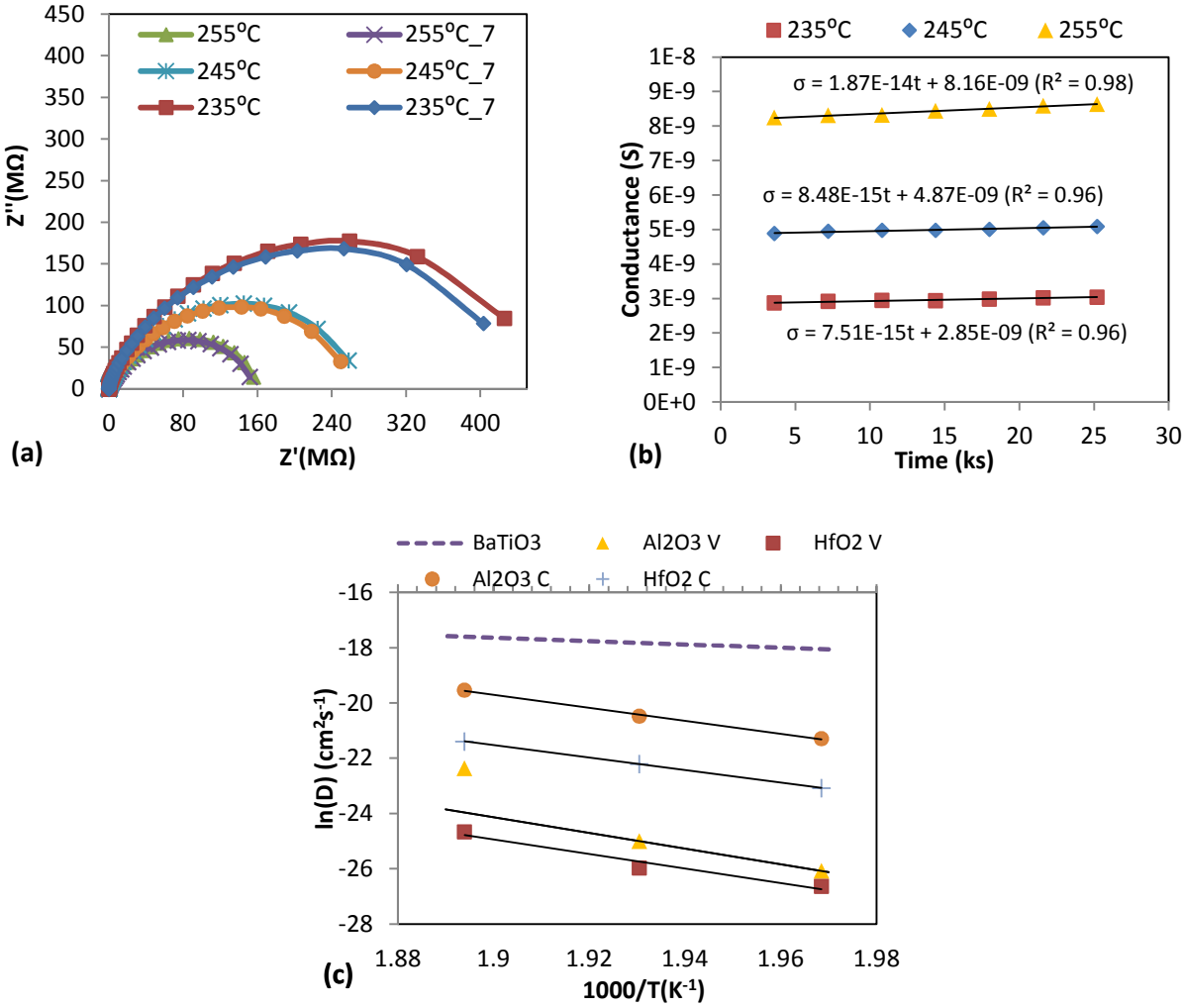

Figure 7 (a) Cole-Cole plots for $BaTiO_3$ capacitor ALD coated with 95 nm of HfO_2 at 235, 245, and 255 °C before and after 7 hours exposer to hydrogen, (b) electrode conductance of the Cole-Cole plots extracted by 3RC model vs time at different temperatures, (c) Proton diffusion coefficient at 235, 245, and 255 °C for ALD coatings of virgin HfO_2, Virgin Al_2O_3 and crystallized HfO_2 and Al_2O_3. For comparison diffusion coefficients in bulk $BaTiO_3$ are given [6].

Table 1 ALD recipes for ZnO, Al_2O_3, and HfO_2 coatings

	ZnO	Al_2O_3	HfO_2
Metal-Precursors	DEZ*	TMA**	TDMAH***
Precursor dose time (s)	0.015	0.03	0.15
Purge time (s)	10	10	10
Water dose time (s)	0.015	0.1	0.03
Purge time (s)	10	10	10
Temperature	200 °C	200 °C	200 °C
Growth rate	1.3 $\dot{A}/cycle$	0.9 $\dot{A}/cycle$	1.1 $\dot{A}/cycle$
Base pressure	300 mtorr	750 mtorr	400 mtorr

* Diethylzinc **Trimethylaluminum *** Tetrakis (dimethylamido) hafnium (IV)

Table 2 Temperature of merit (T_0) in terms of ^oC for Al_2O_3, HfO_2 coatings

	Cycles				
Oxide	110	220	440	660	880
Al_2O_3	-	200	250	270	260
HfO_2	290	310	310	310	310

Table 3 Activation enthalpy (H) and pre-exponential factor (D_0) for amorphous and crystalized materials

Material	Activation Energy (eV)	D_0 (cm^2/s)	reference
α-Al_2O_3 (crystalized)	1.24–1.25	2.4×10^{-3}	46,47
ZrO_2 (crystalized-monoclinic)	0.91	2.4×10^{-7}	48
Si (crystalized)	0.48	2.3×10^{-4}	51
Si (amorphous)	1.4–2.2*	10^{-4}–10^{3}*	52
Al_2O_3 (amorphous)	2.4	8.0×10^{12}	present study
HfO_2 (amorphous)	2.3	7.2×10^{10}	present study
Al_2O_3 (partially crystalized)	2.0	7.7×10^{10}	present study
HfO_2 (partially crystalized)	1.9	2.0×10^{9}	present study

* Both activation energy and pre-exponential factor decrease by increasing hydrogen concentration